PNAS RESEARCH ARTICLE | ENGINEERING ANTHROPOLOGY

Uncovering the crystal defects within aragonite $CaCO_3$

Xingyuan San[a,b,1], Mingyu Gong[c,1], Jian Wang[d,2], Xiuliang Ma[b,2], Roberto dos Reis[e,f], Paul J. M. Smeets[e,f], Vinayak P. Dravid[e,f,2], and Xiaobing Hu[b,e,f,2]

Edited by Lia Addadi, Weizmann Institute of Science, Rehovot, Israel; received December 15, 2021; accepted February 27, 2022

Knowledge of deformation mechanisms in aragonite, one of the three crystalline polymorphs of $CaCO_3$, is essential to understand the overall excellent mechanical performance of nacres. Dislocation slip and deformation twinning were claimed previously as plasticity carriers in aragonite, but crystallographic features of dislocations and twins have been poorly understood. Here, utilizing various transmission electron microscopy techniques, we reveal the atomic structures of twins, partial dislocations, and associated stacking faults. Combining a topological model and density functional theory calculations, we identify complete twin elements, characters of twinning disconnection, and the corresponding twin shear angle (∼8.8°) and rationalize unique partial dislocations as well. Additionally, we reveal an unreported potential energy dissipation mode within aragonite, namely, the formation of nanograins via the pile-up of partial dislocations. Based on the microstructural comparisons of biogenic and abiotic aragonite, we find that the crystallographic features of twins are the same. However, the twin density is much lower in abiotic aragonite due to the vastly different crystallization conditions, which in turn are likely due to the absence of organics, high temperature and pressure differences, the variation in inorganic impurities, or a combination thereof. Our findings enrich the knowledge of intrinsic crystal defects that accommodate plastic deformation in aragonite and provide insights into designing bioengineering materials with better strength and toughness.

biological material | aragonite | crystal defects | organics

Significance

Nacre exhibits outstanding mechanical performance, which results from coordinated deformation mechanisms synergistically working in characteristic microstructures at multiple length scales. A comprehensive understanding of crystal defects within aragonite is critical for discussing the deformation behavior of nacre on microstructure at the nanoscale through atomic scale. By integrating aberration-corrected transmission electron microscopy, crystallographic analysis, and theoretical calculations, we reveal various crystal defects within aragonite at atomic scale and discuss their potential effects on deformation. Our work will serve as cornerstones for modeling analysis and in-depth discussions on nanoscale deformation mechanisms within nacre. Additionally, these atomic-scale insights will benefit theoretical evaluation of the environmental effect on defect formation, enabling defect control in synthetic aragonite and designing of stronger and tougher bioengineering materials.

Aragonite, a metastable crystalline polymorph of $CaCO_3$, is the main component of nacre, occupying ∼95% of the total volume. As a representative natural material, nacre exhibits excellent penetration resistance and the unusual combination of mechanical strength and toughness, three orders of magnitude times higher toughness and two times higher mechanical strength than the main constitute of aragonite (1, 2). Although the unusual mechanical properties of natural materials are mainly ascribed to their hierarchical microstructures (3–6), it is well recognized that mechanical properties of composites are a result of the highly coordinated deformation mechanisms synergistically working in the characteristic microstructures at multiple length scales. Although previous studies mainly focus on the deformation behavior within its brick-and-mortar-like microstructure at the micrometer scale, simulation results show that overall toughness of such hierarchical materials will increase by one order of magnitude when even the fracture toughness of the lowest-level structure is increased by approximately a factor of 2 to 3 (7). Thus, accurate understanding of the deformation mechanisms within aragonite at the smaller length scale (nanoscale through the atomic scale) is essential to appreciate the synergistic effect in nacre and guide the design of stronger and tougher composites. To achieve this, atomic-scale insights of various crystal defects within nacre are a prerequisite.

Dislocation slips and deformation twinning were claimed as plasticity carriers in aragonite but not well understood until now. Kearney et al. conducted nanoindentation tests on single-crystal aragonite with two different tips using atomic force microscopy imaging in tapping mode (8). Through finite element simulations, they postulated that the (110)[001] and ($\bar{1}$10)[001] slip systems could provide the kinematic mechanisms of plastic slip which is necessary to produce the pile-up bands observed in the Berkovich residual impression. It must be pointed out that such speculation cannot rule out other slips and reveal the real Burgers vector. Nonetheless, some researchers found spalling of the tablets at the indentation contact and thus concluded that dislocation-mediated plasticity does not occur within aragonite (9, 10). To date, there is still no direct evidence which visualized dislocations in aragonites. In other aspects, growth twins have been widely observed in aragonite (11–14). For aragonite containing a high density of growth {110} nanotwins, twin boundaries (TBs) can effectively block crack propagation and induce a phase transformation in the vicinity of the crack tip, leading to the delocalization of deformation and

Author contributions: X.M. and X.H. designed research; X.S., M.G., and X.H. performed research; J.W. and X.H. analyzed data; and J.W., X.M., R.d.R., P.J.M.S., V.P.D., and X.H. wrote the paper.

The authors declare no competing interest.

This article is a PNAS Direct Submission.

[1]X.S. and M.G. contributed equally to this work.

[2]To whom correspondence may be addressed. Email: jianwang@unl.edu, xlma@imr.ac.cn, v-dravid@northwestern.edu, or xbhu@northwestern.edu.

This article contains supporting information online at http://www.pnas.org/lookup/suppl/doi:10.1073/pnas.2122218119/-/DCSupplemental.

Published March 31, 2022.

efficient energy dissipation that delays catastrophic fracture (7). In situ transmission electron microscopy (TEM) nanoindentation testing revealed that the preexisting {110} TBs do not migrate (7). Meanwhile, some nanotwins under the indenter are gradually destroyed while other nanograins form due to associated structural transformations in severe local deformation zones. Under high-strain-rate (strain rate $\sim 10^3$/s) uniaxial compression, Huang et al. reported two deformation mechanisms—partial dislocation emission and deformation twinning—in aragonite nanoparticles (15). However, they did not reveal the glide plane and Burgers vector associated with partial dislocations and the twin elements associated with the deformation twinning except the twin plane K_1 = (110), although in the latter the same group and their collaborators attempted to explore the twinning shear process using density functional theory (DFT) calculations (16). Thus, to date, a complete description of deformation twinning and partial dislocations is missing, which limits researchers' deep understanding regarding the intrinsic deformation mechanisms in aragonite.

Here, we uncover the glide plane and Burgers vector of a newly discovered partial dislocation and the complete twin elements of {110} twinning by integrating aberration-corrected scanning TEM (STEM), crystallographic analysis, and first-principles DFT calculations. In addition, we propose a hitherto unreported potential energy dissipation mechanism in aragonite, namely deformation-induced nanograin formation via pile-ups of partial dislocations. Our findings provide insights into structural defects and deformation behavior in aragonite, which will serve as cornerstones for more robust modeling analysis and explorations on the potential external factors (e.g., environmental pressure, temperature, CO_2 concentration, and trace elements) which can be used to tailor the defect density. Benefiting from these atomic scale insights, researchers can further explore the exact relationship between the growth conditions and defect density (17–19) and consequently may be able to design stronger and tougher bioengineering materials through the control of defect density within synthetic aragonite.

Results

Stacking Faults and Partial Dislocations in Aragonite. The macroscopic features and microstructural character of *Pinctada maxima* revealed by X-ray diffraction (XRD) are shown in *SI Appendix*, Fig. S1. The diffraction peaks of the crushed powders are in good agreement with the aragonite crystal structure with space group *Pmcn* and lattice parameters of a = 4.96 Å, b = 7.97 Å, and c = 5.74 Å. The as-obtained *P. maxima* (without crushing the shells) displays evident texture features along the (002) plane. This indicates that the broad surface of *P. maxima* shown in *SI Appendix*, Fig. S1*A* should approximately correspond to the (002) plane. Thus, we prepared electron transparent samples along two distinct directions. One is perpendicular to the broad surface and the other one is parallel to the broad surface. Detailed structural features are revealed in *SI Appendix*, Fig. S2 and Fig. 1. Along the [100] orientation, which is parallel to the broad surface, we can clearly see the representative brick-wall structures of aragonite as shown in *SI Appendix*, Fig. S2*A*. The length of each platelet is around several micrometers, while the thickness is around 200 nm. Serial

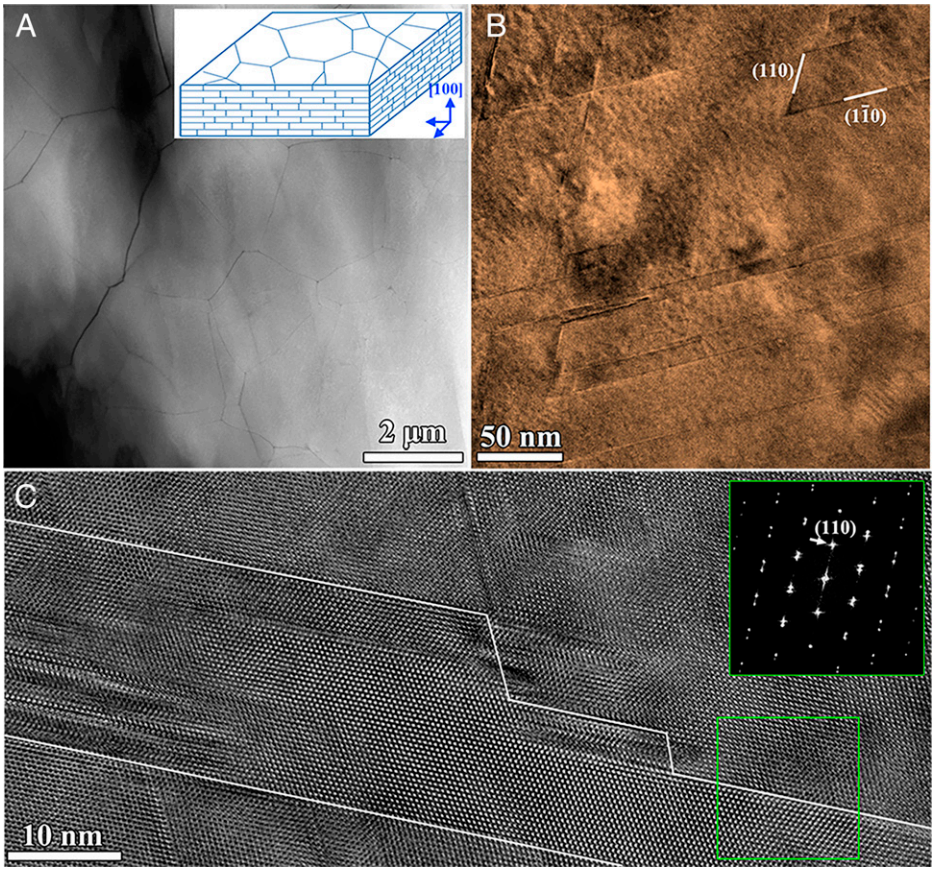

Fig. 1. Structural characterization of the nacre tablet obtained from *P. maxima*. (*A*) A low-magnification HAADF-STEM image showing the grain distributions along the [001] orientation. (*Inset*) A stereo schematic showing the three-dimensional layered aragonite stacking structure of *P. maxima*. (*B*) High-magnification TEM image viewed along the [001] zone axis showing twins and SFs in the grain interior of aragonite. (*C*) HRTEM image of planar defects viewed along the [001] direction. (*Inset*) FFT of the area indicated with the green box.

electron diffraction patterns shown in *SI Appendix*, Fig. S2 *B–E* obtained at different tilt angles can be well-indexed based on the aragonite structure using the above determined lattice parameters using XRD. Along the [001] direction, which is perpendicular to the broad surface of *P. maxima*, we can see the features of columnar grains as shown in Fig. 1*A*. Within the higher-magnification images shown in Fig. 1*B* and *SI Appendix*, Fig. S3, there are plenty of planar defects on (110) and $(1\bar{1}0)$ planes that form an intersection angle of around 64°. These planar defects include both stacking faults and twins (*SI Appendix*, Fig. S3). An atomic-resolution high-angle annular dark field (HAADF) image and corresponding geometrical phase analysis (GPA) of a stacking fault structure is shown in *SI Appendix*, Fig. S4. The stacking fault plane can be determined as {110}. There is a very slight, nearly negligible atomic misalignment across the faulted plane. A high-resolution TEM (HRTEM) image in Fig. 1*C* shows {110} TBs and steps along the TB, respectively, as confirmed by the fast Fourier transform (FFT).

To understand the {110} stacking fault structures, we calculated the γ-surface of the $(1\bar{1}0)$ plane using first-principle DFT calculations. The crystal structure of aragonite and associated projections along some low index directions are shown in *SI Appendix*, Fig. S5. The models shown in Fig. 2 *A–C* with 24 Ca atoms, 24 C atoms, and 72 O atoms adopt the coordinates with the x axis along the [110] direction, the y axis normal to the $(1\bar{1}0)$ plane, and the z axis along the [001] direction. The models have a dimension of $0.947 \times 3.553 \times 0.581$ nm^3. Fig. 2*A1* shows the single crystal in the view normal to the x axis. The crystal is equally divided into R1 and R2 regions with respect to positions along the z axis. Fig. 2 *A2* and *A3* show R1 and R2 regions in the view normal to the z axis. The carbonates are marked by triangles, the corners of which denote positions of O atoms. Thus, carbonates are marked by triangles pointing down in the R1 region and by triangles pointing up in the R2 region. In each region, all Ca atoms or carbonates in the same color (black or purple) have the same z position. In a single-crystal configuration, the yellow solid line is parallel to the (130) plane. The green dashed line across black triangles and the blue dashed line across purple triangles are parallel to the (010) plane. The black and gray dashed lines are parallel to $(1\bar{1}0)$ shear plane. The black dashed line between two nearby Ca layers is denoted as $(1\bar{1}0)^{\#1}$ while the gray dashed line between two Ca layers separated by one carbonate layer is denoted as $(1\bar{1}0)^{\#2}$.

The γ-surface of $(1\bar{1}0)^{\#1}$ plane in Fig. 2*D1* shows two translational vectors, [100] and [110], associated with lattice shear. Fig. 2*D2* shows the energy profiles along the [100] and [110] directions on $(1\bar{1}0)^{\#1}$ plane. It is noted that the [110] shear is decomposed into two 1/2[110] shears, i.e., a full dislocation with the Burgers vector [110] which can be dissociated into two partial dislocations with a Burgers vector 1/2[110]. Correspondingly, Fig. 2*B* shows the fully relaxed stacking fault (SF) structure achieved by 1/2[110] shear on the $(1\bar{1}0)^{\#1}$ plane, referred to as SF_{CO_3}. The associated SF energy (SFE) is 49.6 mJ/m^2. It should be noted that the sublattice of Ca atoms does not show faulted stacking. The faulted structure is only associated with the faulting of carbonates. Therefore, the SF_{CO_3} can only be observed at low magnification in TEM mode due to the local strain contrast along the SF_{CO_3}. However, when imaging at atomic resolution, the SF_{CO_3} cannot be observed since faulted C and O atoms with relatively low atomic number do not have sufficient contrast. This is consistent with our experimental observations shown in *SI Appendix*, Fig. S4.

In addition to the above-mentioned SF_{CO_3}, there is another type of possible SF. Fig. 2*E* shows the energy profile along [110] direction on $(1\bar{1}0)^{\#2}$ plane. The two metastable points at 1/2[110] and 0.28[110] correspond to two SFs. Fig. 2*C1* shows the faulted structure achieved by 1/2[110] shear on $(1\bar{1}0)^{\#2}$ plane, which is equivalent to the SF_{CO_3} as shown in Fig. 2*B*. There is another possible faulted structure created by 0.28[110] shear on the $(1\bar{1}0)^{\#2}$ plane, referred to as SF_{Ca}. After full relaxation, the SFE associated with SF_{Ca} is calculated as 426.8 mJ/m^2. It should be noted that both Ca atoms and carbonates show faulted stackings, implying that SF_{Ca} can be observed in atomic-resolution images.

Compared to the SFEs of two possible stacking faulted structures, SFE associated with SF_{CO_3} is comparable to the SFE of Cu (~41 mJ/m^2) which contains a high density of growth twins and SFs. Thus, the high density of SF_{CO_3} may form during the growth process of nacre and is likely associated with the glide of 1/2[110] partial dislocations during mechanical loading. However, a lower density of SF_{Ca} may only form during growth and mechanical loading of nacre because of its high SFE and greater energy barrier.

{110} Twinning in Aragonite. We further obtained atomic-resolution HAADF-STEM images of several twin structures along the [001] direction of aragonite. Since the HAADF imaging technique provides atomic number (Z) contrast with intensities proportional to $Z^{1.7\sim1.9}$ (20–22), the bright contrast columns indicate the positions of Ca atoms and light elements such as C and O are invisible in the images. Ca atoms form a pseudo-hexagonal close-packed structure, which poses some difficulty in distinguishing it from a perfect hexagonal crystal in atomic-resolution images. Fig. 3*A* shows an atomic-resolution HAADF image of a flat TB and Fig. 3*B* shows a two-layer-thick twin structure. The twinning plane is determined to be {110} according to the selected area diffraction patterns and digital FFT patterns (Fig. 1*C* and *SI Appendix*, Fig. S3*B*). In order to accurately describe the twin structure, five quantities including K_1, η_1, K_2, and η_2 and the corresponding twinning angle α are needed. Based on experimental observations, the quantity K_1 can be determined as (110). However, the other quantities cannot be identified by only carrying out the experiment. Fig. 3*C* shows a twin with one step and the step height is one atomic layer d_0. Fig. 3*D* shows a twin with two steps as clearly revealed in *SI Appendix*, Fig. S6*B* by strain analysis using GPA. The step height is approximately seven to eight atomic layers and the magnitude of the net Burgers vector associated with the step is about 1/2[110] according to the Burgers circuits 1 and 2. Additionally, Fig. 3*E*, an HRTEM image along the [001] direction, shows another twin structure with irrational boundaries. Similarly, dislocations are frequently revealed along the TBs and the net Burgers vector can be determined as 1/2[110] according the Burgers circuits drawn on Fig. 3*F*. The distance between neighboring dislocations is around 3.8 nm, which is approximately seven to eight atomic layers.

In order to gain a deeper understanding of the {110} twinning in aragonite $CaCO_3$, we performed DFT calculations and elaborate crystallographic analysis. Fig. 4*A* is a $2 \times 1 \times 1$ periodic image showing a matrix crystal (lower part), a twin crystal (upper part), and a K_1 TB in the center. The twin crystal is rotated 180° of the matrix crystals about the normal of the twin plane. The K_1 TB is fully coherent and is thus referred to as a coherent TB (CTB). The model with 20 Ca atoms, 20 C atoms, and 60 O atoms adopts the coordinates of the x axis along the [110] direction, the y axis normal to the $(1\bar{1}0)$ plane, and the z axis along the [001] direction to have a dimension of $0.947 \times 2.553 \times 0.581$ nm^3. The dotted black and red rectangles represent the primitive cells in matrix and twin. Each

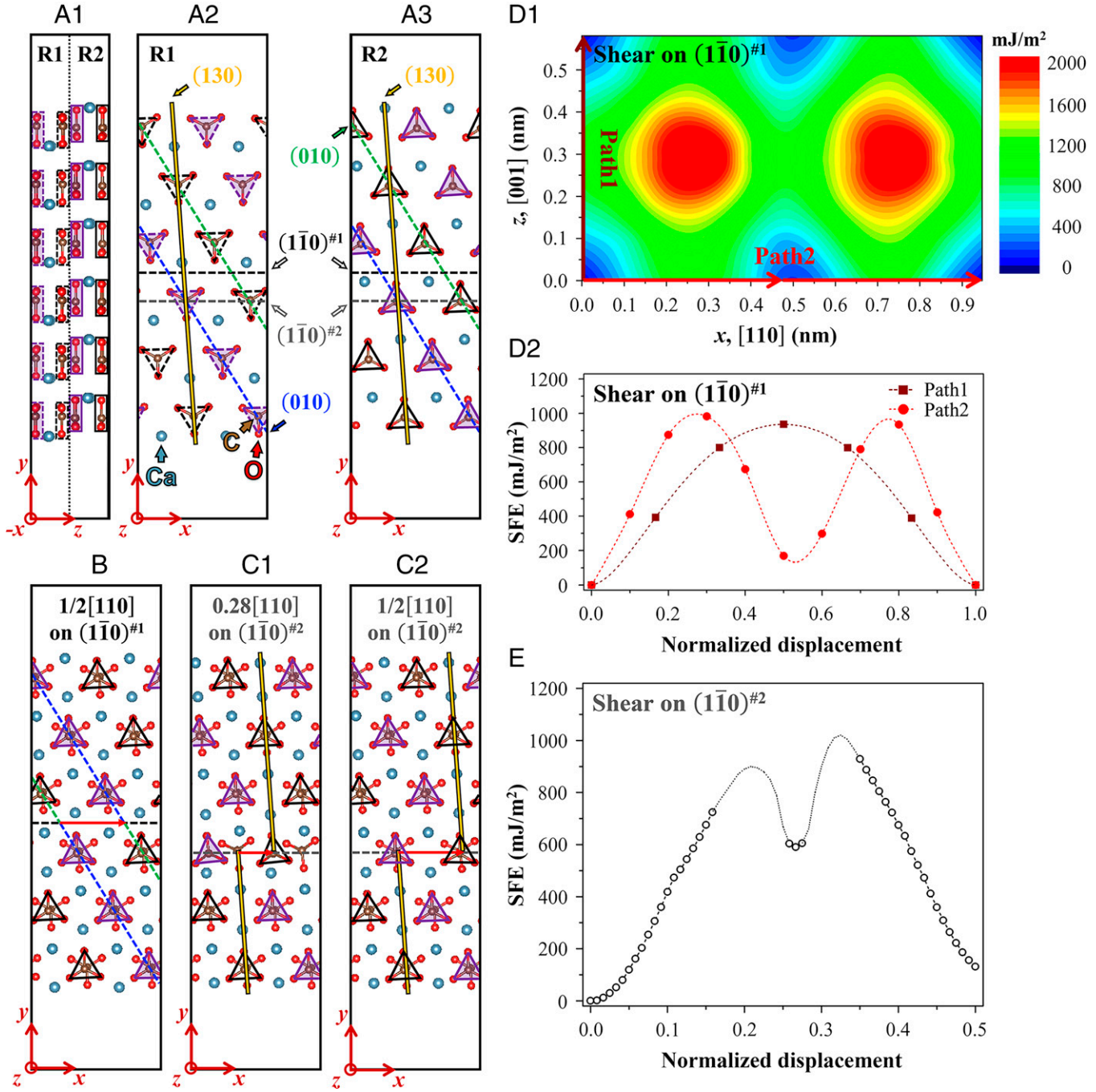

Fig. 2. Theoretical calculations of the possible SF structures within aragonite. (A_1) Atomic configuration of a single crystal observed along the [110] axis. Atomic configurations of (A_2) R1 region and (A_3) R2 region observed along the [001] axis. In this schematic, *x*, *y*, and *z* axis is along [110], ~[5$\bar{2}$0] (normal to (1$\bar{1}$0) plane), and [001] direction, respectively. (*B*) Atomic configuration of SF_{CO_3} created by 1/2[110] shear on $(1\bar{1}0)^{\#1}$ plane viewed along the [001] axis. Atomic configurations viewed along the [001] axis of (C_1) SF_{Ca} created by 1/2[110] shear on $(1\bar{1}0)^{\#2}$ plane and (C_2) SF_{Ca} created by 0.28[110] shear on $(1\bar{1}0)^{\#2}$ plane. (D_1) γ-surface on $(1\bar{1}0)^{\#1}$ plane. (D_2) Energy profiles along Path1 and Path2. (*E*) Energy profile associated with shear along [110] on $(1\bar{1}0)^{\#2}$ plane.

primitive cell contains 4 Ca atoms, 4 C atoms, and 12 O atoms. Crystallographic analysis was performed using the topological model (23–25). Fig. 4 *B* and *C* show the dichromatic pattern and complex associated with (1$\bar{1}$0) twinning with the coordinate, the same as that of the atomic model (Fig. 4*A*). In Fig. 4*B*, solid and open blue squares represent lattice sites in matrix and twin, respectively. Each lattice point contains a primitive cell. In Fig. 4*C*, the black and red symbols represent atoms in matrix and twin, respectively. Circles represent Ca atoms while triangles represent carbonates. Three corners of the triangle correspond the positions of three O atoms of a carbonate (CO_3), and one C atom occupies the center of the triangle. The horizontal brown dashed line represents the CTB. Corresponding to the upward migration of the CTB, atoms/lattices in the matrix orientation will be moved to atoms/lattices in a twin orientation through shear and shuffle associated with the glide of twinning disconnections (TDs). Burgers vectors of possible one-layer TD $b_{1/1}$ and two-layer TD $b_{2/2}$ are defined in the dichromatic pattern (Fig. 4*B*), which are 0.44[1$\bar{1}$0] (with magnitude of 0.42 nm) and 0.12[110] (with magnitude of 0.11 nm), respectively. TDs with higher step can always decompose into $b_{1/1}$ and $b_{2/2}$. Since the magnitude of $b_{1/1}$ is much larger than $b_{2/2}$, nucleation of $b_{2/2}$ should be easier. DFT calculations further demonstrated that a two-layer-thick twin (Fig. 2*D*) is stable while a one-layer-thick

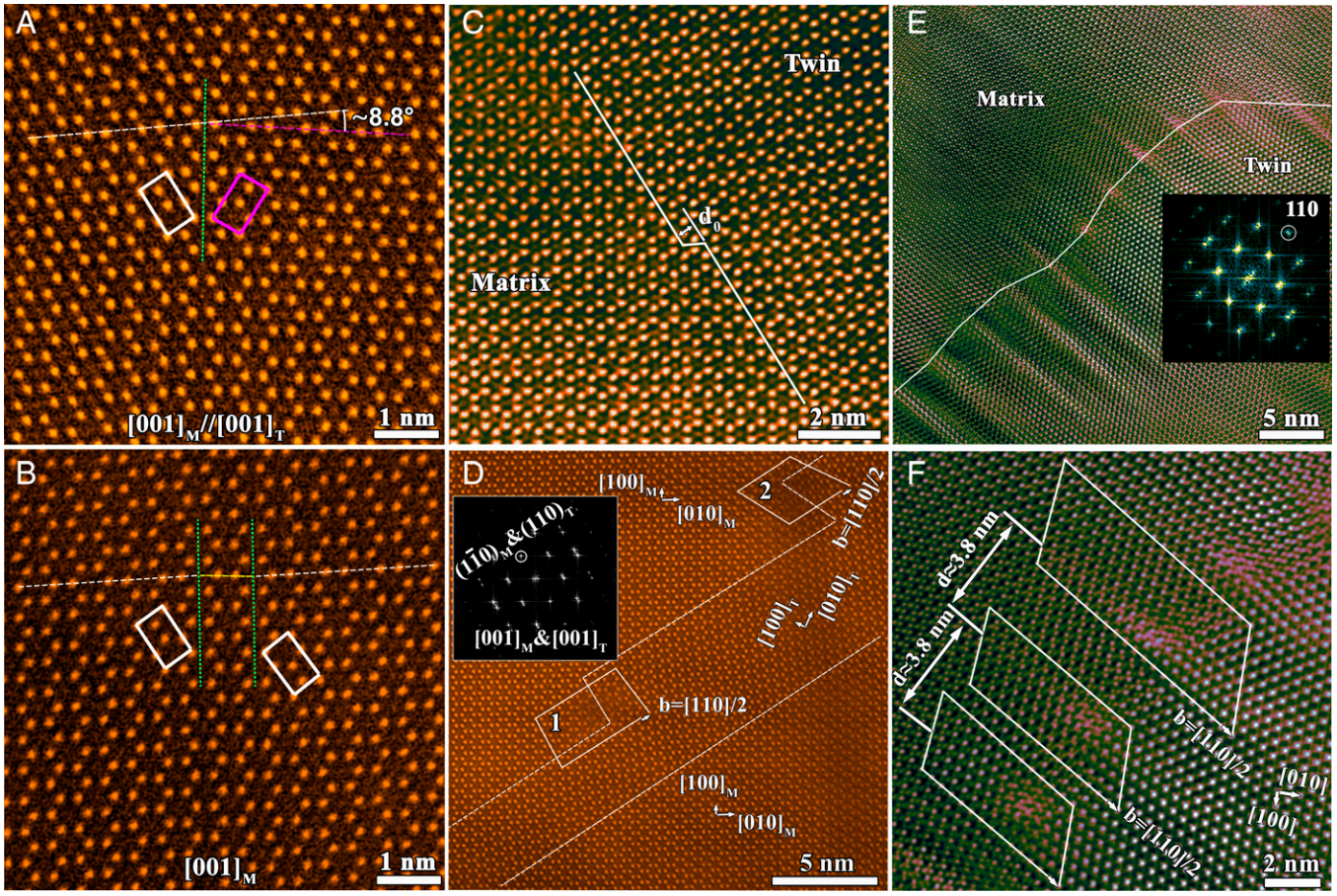

Fig. 3. Atomic-scale observations of the twinning structure and associated dislocations on TB. Atomic-resolution HAADF image of (*A*) the bulk twin structure and (*B*) a two-layer twin structure along the [001] direction. The rectangle frames in *A* and *B* outline the unit cell in aragonite. The twin angles are indicated as well. Atomic-resolution HAADF image of the twin with (*C*) one layer thickness and (*D*) varied thickness. The dislocations associated with TB are indicated using the Burgers vector circuits. (*Inset*) FFT patterns correspond to a twin structure of aragonite. The Burgers vector is determined as 1/2[110]. (*E*) HRTEM image of a twin structure with an irrational TB. (*F*) Local magnification of TB area in *E* showing the dislocations on the boundary.

twin is unstable and will eventually further develop into a two-layer twin structure. So, $(1\bar{1}0)$ twinning should be accomplished by nucleation and glide of two-layer TDs $b_{2/2}$. Therefore, the twin shear direction (η_1) is [110], the Burgers vector of TDs (b) is 0.12[110], and the step height (h) is 2. The associated characteristic twin shear is thus calculated to be $s = |b|/h = 0.14$. The K_2 plane is determined to be (130) planes as indicated by the solid lines (yellow and white) in the matrix and twin domain in Fig. 4*B*. The angles between two (130) planes on two sides of the CTB is 172.6°, thus the shear angle (2α) is 7.4°, which agrees well with the experimental observation shown in Fig. 3*A*. The conjugate twin shear direction (η_2) is $[\bar{3}10]$. The interface energy of CTB is calculated based on the model shown in Fig. 4*A*, which is 5.01 mJ/m^2. The extremely low TB energy can well account for the formation of massive growth twins as revealed in Fig. 1 *B* and *C*.

Crystallographic analysis and DFT calculations confirm that $(1\bar{1}0)$ twinning is operated by successive nucleation and glide of two-layer TDs. Thus, the net Burgers vector (1/2[110]) associated with the step can be understood as the pile-up of TDs. The ratio of $b_p/b_{2/2} \approx 4.27$, which corresponds to the pile up of at least four TDs. The corresponding height is eight atomic layers, which is consistent with the step height in Fig. 3*F*. A coherent dichromatic pattern in *SI Appendix*, Fig. S6*C* shows stress-free twin steps with one 1/2[110] dislocation which was formed by eight $(1\bar{1}0)$ layers. In this sense, the mechanism associated with $(1\bar{1}0)$ twinning in aragonite $CaCO_3$ is different from the mechanism associated with successive glide of Shockley partial dislocations on {111} twin planes in face-centered cubic metals. Plasticity associated with twinning could be accomplished by thickening growth twins or nucleating deformation twins via nucleation and glide of $b_{2/2}$ TDs on the TB.

Discussion

The possible slip systems of (110)[001] were proposed based on the crystal structure and speculation on deformation behaviors. Intuitively, the shortest translation vector in aragonite is [100] with the magnitude of ~0.5 nm. The [001] direction has a larger distance with the magnitude of ~0.57 nm. The [110] direction was never considered to be a possible shear vector because it is too large, about 0.94 nm. However, the unique partial dislocations on the {110} glide plane with Burgers vector 1/2[110] identified here have a shorter magnitude of ~0.47 nm. More importantly, the stacking fault structure associated with the glide of the partial dislocation has a lower fault energy ~49.60 mJ/m^2. This should account for the presence of SFs. Moreover, it is speculated that some boundaries may form associated with pile-up of partial dislocations in aragonite if the unique partial dislocations are activated during deformation. Interestingly, we observed such kinds of grain boundaries (GBs) associated with formation of nanosized grains (Fig. 5*A* and *SI Appendix*, Figs. S7 and S8). The misorientation angle is less than 10° and the misorientation axis is the [001] zone axis.

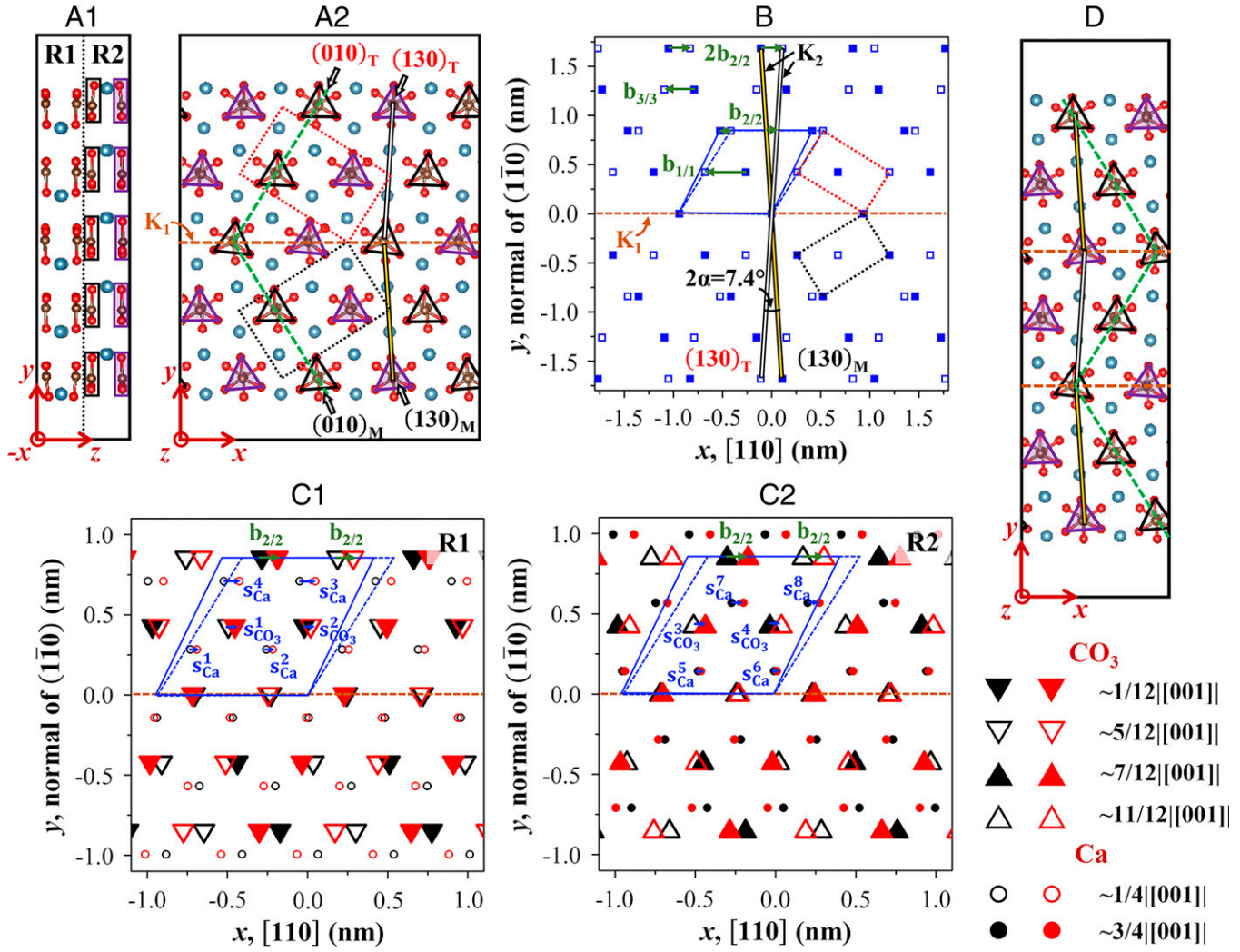

Fig. 4. Crystallographic account of the twinning structure within aragonite. A 2 × 1 × 1 periodic image of the simulated atomic configuration with a TB observed along (A_1) [110] axis and (A_2) [001] axis. (*B*) Coherent dichromatic pattern of (1$\bar{1}$0) twinning. Coherent dichromatic complex of (1$\bar{1}$0) twinning in (C_1) R1 region and (C_2) R2 region along the [001] direction. (*D*) Atomic configuration of a two-layer twin viewed along the [001] axis.

Fig. 5*A* shows a 20-nm nanograin. The atomic-resolution HAADF images shown in Fig. 5 *B* and *C* reveal structural details of the GB. The digital FFT patterns shown in Fig. 5*B*, Inset indicates a ∼6.8° deflection across the GB highlighted by shaded curves between the (110) planes. Along the GB, an array of dislocations can be identified. Some cores of the dislocations can be well revealed due to a pure rotation operation along the [001] zone axis. As indicated in the Burgers circuits shown in atoms resolved images in Fig. 5*C*, the Burgers vector of these dislocations can be determined as 1/2[110]. The tilt GB dislocations visualized in atomic-resolution HAADF images (Fig. 5*B*) are responsible for the in-plane rotation. The average spacing between the adjacent dislocations along the tilt GB is measured to be L ∼3.9 nm. According to Frank–Bilby equation, the calculated tilt angle is ∼7° [$\theta = \sin^{-1}(b/L)$], where b (∼0.47 nm) is the length of the Burgers vector 1/2 <110>. The calculated rotation angle is consistent with our experimental observations. Another representative nanograin structure with a rotation angle of around 9° is shown in *SI Appendix*, Fig. S7 as well. Thus, we rationalize the formation of nanograins as follows. Corresponding to the characters of GB dislocations in Fig. 5, the nucleation of nanograins at GBs is most likely accommodated by the 1/2[110] partial dislocations. A schematic of the formation mechanisms is shown in Fig. 5*D*. Arrays of partial dislocations may nucleate at GBs or surfaces and glide on {110} planes toward the grain interior. These partial dislocations pile up and form dislocation walls, which finally result in the formation of a nanograin. Corresponding to this mechanism, a high density of SFs should be present in the nanograin, as observed in the low-magnification HAADF-STEM image (Fig. 5*A*). However, such SFs cannot be identified in the atomic-resolution HAADF image (Fig. 5*B*), because the image only shows the sublattice of Ca.

{110} twins have been widely observed in aragonite but not completely understood yet. Combined with the crystallographic analyses and DFT calculations based on atomic-scale characterizations, we uncover the complete twin elements [K_1 = (1$\bar{1}$0), η_1 = [110], K_2 = (130), η_2 = [$\bar{3}$10]), the characters of TD (b = 0.11[110], h = 2] and twin shear angle (∼8.8°). The step height of the TD contains two {110} atomic layers. The burgers vector associated with the TD is ∼0.12[110], which is about one-quarter of the 1/2[110]{1$\bar{1}$0} partial dislocation. Due to the small Burgers vector, it is impossible to identify a single TD. Steps will form associated with TDs pile-up. These TDs will resemble one visible lattice dislocation with a Burgers of 1/2[110]. For preexisting TBs associated with growth twins, nucleation and glide of TDs on the TB will thicken twins, accommodating plastic deformation.

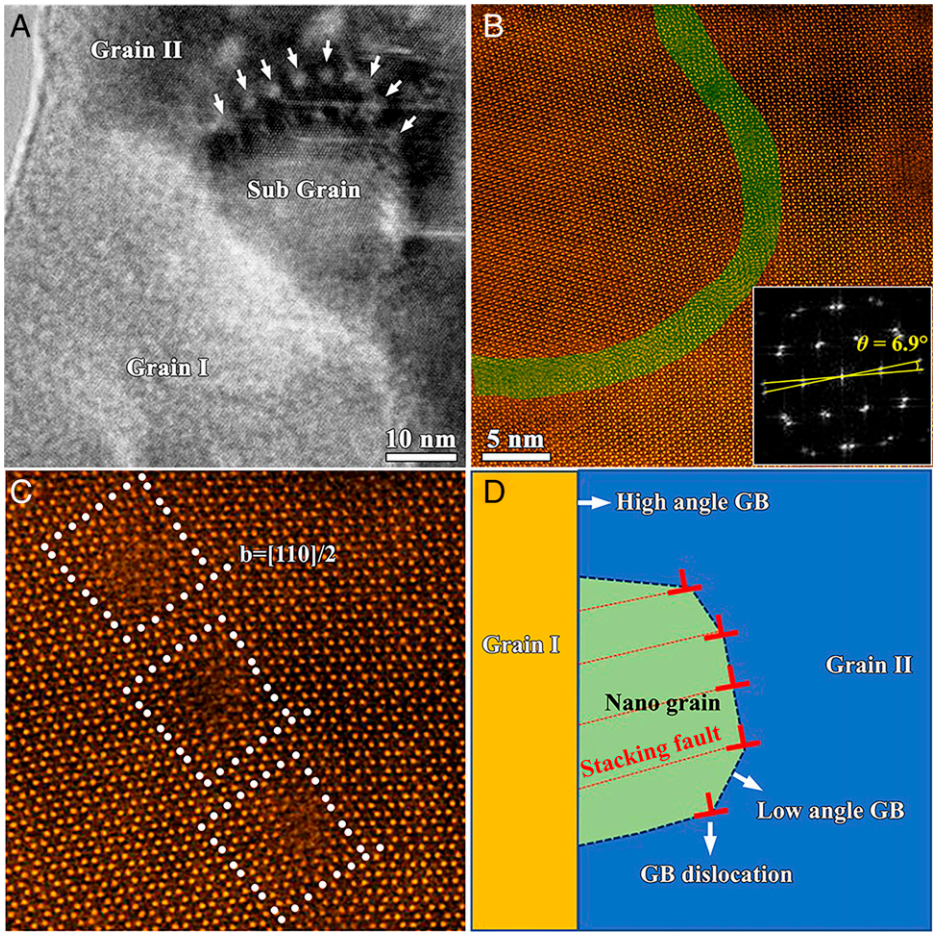

Fig. 5. Formation mechanism of nanosized grains neighboring a GB. (*A*) A low-magnification HAADF image showing formation of a subgrain between grain I and II. White arrows denote the dislocation along a low-angle GB (LAGB). (*B*) Atomic-resolution HAADF image of a LAGB highlighted by shaded curves. *Inset* is the corresponding digital FFT patterns. (*C*) Localized magnification of the area along GB showing the existence of GB dislocations. The Burgers vector *b* is determined as 1/2[110]. (*D*) Schematic for the formation mechanisms of the LAGB.

All above-mentioned crystal defects are obtained from biogenic aragonite materials. To compare with the structural defects of abiotic aragonite, we performed further studies on the geological aragonite minerals which originate from Morocco. The general structural features are shown in *SI Appendix*, Fig. S9. It is found that a sporadic twinning structure which has the same feature as the one in the biogenic structure indeed existed in the abiotic mineral, but its twinning density appears very low in the abiotic mineral (*SI Appendix*, Figs. S9 and S10). In biogenic aragonite materials, the representative feature is the existence of the organics. High-magnification HAADF images (*SI Appendix*, Fig. S11 *A* and *B*) demonstrate clear contrast inhomogeneity. The dark area along the boundary and small areas with dark contrast in grain interior indicate a relative lower average atomic number. Thus, these areas likely correspond to inter- and intracrystalline organics, respectively (26). A semiquantitative elements analysis (*SI Appendix*, Fig. S11*C*) reveals that the darker-contrast area has a relative higher C/Ca ratio in comparison to the brighter area, which is another supportive evidence for the organics. The atomic-resolution TEM image shown in *SI Appendix*, Fig. S11*D* shows that the crystallinity of the dark areas is very poor, which is reasonable considering the existence of intracrystalline organics. In previous work, researchers have demonstrated that the organics play a critical role in many aspects in biogenic materials, such as directing the mineralization (27), causing isotropic lattice distortions in biogenic aragonite and calcite (28–32), and formation of unique twin structure in biogenic calcite (33). Since abiotic aragonite minerals are free of organics, it is reasonable to deduce that both the intra- and intercrystalline organics play a critical role in defect formation in biogenic aragonite materials. Internal stress, which can result from either the formation of organics within biogenic nacre or volume changes during the transformation process from amorphous $CaCO_3$ to crystalline aragonite, likely promotes the formation of many defect structures in nacre. Further large-scale theoretical work is still needed to reveal the relationship between organics and defects formation. Besides the biological effect, trace elemental impurities may be another factor that can affect the formation of defect structure within aragonite. Any impurity elements that can reduce the energy of the stacking faults and twin structures will promote the formation of various structural defects in aragonite as well. Therefore, our atomic-scale insights of the defects structure allow researchers to theoretically evaluate the potential effects of the impurity elements on the energy of various defect structures, which may enable researchers to control the defect density within biogenetic aragonite during growth process.

Materials and Methods

Sample Preparation and Electron Microscopy Methods. The biogenic aragonite materials used in the present work are shells of *P. maxima* which were collected from the South China Sea. The abiotic geological aragonite minerals were purchased online and originated from Morocco. To minimize the detrimental effect of collision and dehydration on the structure and mechanical behavior of the shells, they were kept in the refrigerator in the laboratory. To investigate

the characteristics of the defect structures within aragonite mineral, *P. maxima* were cut along different orientations. Thin foils were prepared with a diamond saw and then mounted on a Mo grid. Then, the foils were mechanically polished using silicon carbide papers to the thickness of ~30 μm and further dimpled to <10 μm. The electron transparent foils were finally prepared by Ar ion milling in a Gatan precision ion polishing system using a low voltage (3 to 4 kV) to avoid any possible ion beam damage. Then, the electron transparent specimens were coated with carbon (~30 nm) to enhance the electron conductivity using Carbon Evaporator (Q150RE-Plus; Quorum, Inc).

XRD data were acquired using the Bede D1 system with Cu-K_a radiation (λ = 0.15406 nm). The selected area electron diffraction patterns, bright-field and dark-field images, and atomic-resolution TEM and HAADF images were obtained using a probe-corrected JEOL ARM 200CF microscope. This microscope equipped with a CEOS probe corrector and the cold-field emission gun was operated at 200 kV. The convergence semiangle used in STEM mode is around 22 mrad and the collection semiangle for HAADF imaging ranged from 90 to 370 mrad. Within this high angle range, the intensity of images is dominated by incoherent *Z* contrast. Additionally, this microscope was equipped with dual silicon drift detectors with an area of a single detector covering 100 mm^2. The achievable solid angle for energy dispersive spectrum analysis is around 1.7 sr.

DFT Calculations. For better interpreting the experimental observations, we performed first-principles simulations with the Vienna ab initio simulation package (VASP), with specific emphasis on elucidating the lattice angle differences between the asymmetric TBs.

Optimization of lattice parameters. The generalized gradient approximation with Perdew–Burke–Ernzerhof parameterization was used for the exchange and correlation functions (34). The core electrons were replaced by the projector augmented wave pseudopotentials (35) with the valence states $3s^23p^64s^2$, $2s^22p^2$, and $2s^22p^4$ for Ca, C, and O, respectively. A 500-eV cutoff on kinetic energy was used for the plane wave basis set. During calculations, the self-consistent iteration was stopped when the change of total energy was smaller than 10^{-5} eV. The convergence criterion of geometry optimizations was that the forces acting on each atom is smaller than 0.01 eV/Å. With the first Brillouin zone for unit cells of aragonite $CaCO_3$ sampled by 9 × 6 × 8 Monkhorst-Pack (M-P) K-point grids (36), the optimized lattice parameters are a = 5.016 Å, b = 8.035 Å, and c = 5.812 Å and the cohesive energy is −2.467 eV per atom.

Calculation of γ-surface. The calculation of γ-surface on the {110} plane started from the single crystal structure containing 24 Ca atoms, 24 C atoms, and 72 O atoms as shown in Fig. 2*A* with *x* axis along the [110] direction, *y* axis normal to the $(1\bar{1}0)$ plane, and *z* axis along the [001] direction. The model has a dimension of 0.947 × 3.553 × 0.581 nm^3. Thus, the area (*A*) of the {110} plane is 0.947 × 0.581 nm^2. During relaxation, periodic boundary conditions were applied in *x* and *z* directions, atoms on the top and bottom $(1\bar{1}0)$ layers were fixed, and the other atoms could relax in all directions. The first Brillouin zone was integrated by 4 × 1 × 6 M-P K-points. The total energy associated with the relaxed model with perfect stackings is denoted as E_p. Then, the structure containing faulted stacking was created by shearing the single-crystal model on the $(1\bar{1}0)$ plane with certain displacement. During relaxation of faulting structures, atoms on the top and bottom $(1\bar{1}0)$ layers were fixed while the other atoms could move in the *y* direction. The total energy associated with the relaxed model with faulted stacks is denoted as E_f. SFE is thus calculated as

$$\mathrm{SFE} = \frac{\mathrm{E_f} - \mathrm{E_p}}{\mathrm{A}}. \quad [1]$$

A 10 × 6 grid was applied to the $(1\bar{1}0)$ shear plane, and SFE associated with each grid point is calculated and shown in Fig. 2 *D* and *E*.

Calculation of interface energy of CTB. To calculate the interface energy associated with CTB, model 1 containing one CTB and two $(1\bar{1}0)$ free surfaces (as shown in Fig. 4*A*) and model 2 only containing two $(1\bar{1}0)$ free surfaces were constructed. Both models contain 20 Ca atoms, 20 C atoms, and 60 O atoms, adopt the coordinates that *x* axis along the [110] direction, *y* axis normal to the $(1\bar{1}0)$ plane, and *z* axis along the [001] direction, and have dimensions 0.947 × 2.553 × 0.581 nm^3. Thus, the area (*A*) of CTB is 0.947 × 0.581 nm^2. During relaxation, periodic boundary conditions were applied in *x* and *z* directions, atoms on the top and bottom $(1\bar{1}0)$ layers were fixed, and the other atoms could fully relax. With the first Brillouin zone integrated by 4 × 1 × 6 M-P K-points, the total energies were calculated as E_1 and E_2 for models 1 and 2. The interface energy of CTB (E_{CTB}) is calculated as

$$E_{CTB} = \frac{\mathrm{E_1} - \mathrm{E_2}}{\mathrm{A}}. \quad [2]$$

Data Availability. All study data are included in the article and/or *SI Appendix*.

ACKNOWLEDGMENTS. X.H. thanks Dr. S. Hao at Northwestern University and Dr. Q. Q. Ren at Oak Ridge National Laboratory for helpful discussions. This work was supported by the National Natural Science Foundation of China (Grant 51901065), the Nature Science Foundation of Hebei Province (Grant E2020201023), and Advanced Talents Incubation Program of the Hebei University (Grant 521000981164). This work made use of the EPIC facility of Northwestern University's NU*ANCE* Center, which has received support from the Soft and Hybrid Nanotechnology Experimental (SHyNE) Resource (NSF Grant ECCS-2025633), the International Institute of Nanotechnology (IIN), and Northwestern's Materials Research Science and Engineering Center (MRSEC) program (NSF Grant DMR-1720139).

Author affiliations: [a]Hebei Key Laboratory of Optic-electronic Information and Materials, The College of Physics Science and Technology, Hebei University, Baoding 071002, China; [b]Shenyang National Laboratory for Materials Science, Institute of Metal Research, Chinese Academy of Sciences, Shenyang 110016, China; [c]State Key Laboratory of Metal Matrix Composites, School of Materials Science and Engineering, Shanghai Jiao Tong University, Shanghai 200240, China; [d]Department of Mechanical and Materials Engineering, University of Nebraska–Lincoln, Lincoln, NE 68583; [e]Department of Materials Science and Engineering, Northwestern University, Evanston, IL 60208; and [f]The Northwestern University Atomic and Nanoscale Characterization Experimental Center, Northwestern University, Evanston, IL 60208

1. R. Z. Wang, Z. Suo, A. G. Evans, N. Yao, I. A. Aksay, Deformation mechanisms in nacre. *J. Mater. Res.* **16**, 2485–2493 (2001).
2. F. Barthelat, C.-M. Li, C. Comi, H. D. Espinosa, Mechanical properties of nacre constituents and their impact on mechanical performance. *J. Mater. Res.* **21**, 1977–1986 (2006).
3. K. S. Katti, D. R. Katti, S. M. Pradhan, A. Bhosle, Platelet interlocks are the key to toughness and strength in nacre. *J. Mater. Res.* **20**, 1097–1100 (2005).
4. U. G. Wegst, H. Bai, E. Saiz, A. P. Tomsia, R. O. Ritchie, Bioinspired structural materials. *Nat. Mater.* **14**, 23–36 (2015).
5. H.-C. Loh *et al.*, Nacre toughening due to cooperative plastic deformation of stacks of co-oriented aragonite platelets. *Commun. Mater.* **1**, 77 (2020).
6. H. D. Espinosa *et al.*, Tablet-level origin of toughening in abalone shells and translation to synthetic composite materials. *Nat. Commun.* **2**, 173 (2011).
7. Y. A. Shin *et al.*, Nanotwin-governed toughening mechanism in hierarchically structured biological materials. *Nat. Commun.* **7**, 10772 (2016).
8. C. Kearney *et al.*, Nanoscale anisotropic plastic deformation in single crystal aragonite. *Phys. Rev. Lett.* **96**, 255505 (2006).
9. S. Wang, X. Zhu, Q. Li, R. Wang, X. Wang, Damage-tolerance strategies for nacre tablets. *J. Struct. Biol.* **194**, 199–204 (2016).
10. H. Gopalan, A. H. Chokshi, The mechanical behavior of nacre across length scales. *J. Mech. Behav. Biomed. Mater.* **78**, 96–107 (2018).
11. W. A. Wooster, Atomic arrangements on the twin boundaries of crystals of calcite and aragonite. *Mineral. Mag.* **46**, 265–268 (1982).
12. H. Mukai, K. Saruwatari, H. Nagasawa, T. Kogure, Aragonite twinning in gastropod nacre. *J. Cryst. Growth* **312**, 3014–3019 (2010).
13. M. Suzuki, H. Kim, H. Mukai, H. Nagasawa, T. Kogure, Quantitative XRD analysis of 110 twin density in biotic aragonites. *J. Struct. Biol.* **180**, 458–468 (2012).
14. M. E. Marsh, R. L. Sass, Aragonite twinning in the molluscan bivalve hinge ligament. *Science* **208**, 1262–1263 (1980).
15. Z. Huang *et al.*, Uncovering high-strain rate protection mechanism in nacre. *Sci. Rep.* **1**, 148 (2011).
16. J. Liu *et al.*, Atomistic origin of deformation twinning in biomineral aragonite. *Phys. Rev. Lett.* **118**, 105501 (2017).
17. T. Kogure *et al.*, Twin density of aragonite in molluscan shells characterized using X-ray diffraction and transmission electron microscopy. *J. Cryst. Growth* **397**, 39–46 (2014).
18. L. S. Gomez-Villalba, P. López-Arce, M. Alvarez de Buergo, R. Fort, Atomic defects and their relationship to aragonite–calcite transformation in portlandite nanocrystal carbonation. *Cryst. Growth Des.* **12**, 4844–4852 (2012).
19. V. L. Peck, R. L. Oakes, E. M. Harper, C. Manno, G. A. Tarling, Pteropods counter mechanical damage and dissolution through extensive shell repair. *Nat. Commun.* **9**, 264 (2018).
20. S. J. Pennycook, D. E. Jesson, High-resolution incoherent imaging of crystals. *Phys. Rev. Lett.* **64**, 938–941 (1990).
21. P. D. Nellist, S. J. Pennycook, The principles and interpretation of annular dark-field Z-contrast imaging. *Adv. Imaging Electron Phys.* **113**, 147–203 (2000).
22. S. J. Pennycook, Structure determination through Z-contrast microscopy. *Adv. Imaging Electron Phys.* **123**, 173–206 (2002).
23. J. P. Hirth, J. Wang, C. N. Tomé, Disconnections and other defects associated with twin interfaces. *Prog. Mater. Sci.* **83**, 417–471 (2016).

24. J. P. Hirth, R. C. Pond, R. G. Hoagland, X. Y. Liu, J. Wang, Interface defects, reference spaces and the Frank–Bilby equation. *Prog. Mater. Sci.* **58**, 749–823 (2013).
25. R. C. Pond, X. Ma, Y. W. Chai, J. P. Hirth, "Topological modelling of martensitic transformations" in *Dislocations in Solids*, F. R. N. Nabarro, J. P. Hirth, Eds. (Elsevier, 2007), vol. **13**, chap. 74, pp. 225–261.
26. K. Gries, R. Kröger, C. Kübel, M. Fritz, A. Rosenauer, Investigations of voids in the aragonite platelets of nacre. *Acta Biomater.* **5**, 3038–3044 (2009).
27. P. J. M. Smeets, K. R. Cho, R. G. Kempen, N. A. Sommerdijk, J. J. De Yoreo, Calcium carbonate nucleation driven by ion binding in a biomimetic matrix revealed by *in situ* electron microscopy. *Nat. Mater.* **14**, 394–399 (2015).
28. B. Pokroy, J. P. Quintana, E. N. Caspi, A. Berner, E. Zolotoyabko, Anisotropic lattice distortions in biogenic aragonite. *Nat. Mater.* **3**, 900–902 (2004).
29. B. Pokroy *et al.*, Anisotropic lattice distortions in biogenic calcite induced by intra-crystalline organic molecules. *J. Struct. Biol.* **155**, 96–103 (2006).
30. B. Pokroy *et al.*, Anisotropic lattice distortions in the mollusk-made aragonite: A widespread phenomenon. *J. Struct. Biol.* **153**, 145–150 (2006).
31. E. Seknazi, B. Pokroy, Residual strain and stress in biocrystals. *Adv. Mater.* **30**, e1707263 (2018).
32. B. Pokroy, A. Fitch, E. Zolotoyabko, The microstructure of biogenic calcite: A view by high-resolution synchrotron powder diffraction. *Adv. Mater.* **18**, 2363–2368 (2006).
33. B. Pokroy, M. Kapon, F. Marin, N. Adir, E. Zolotoyabko, Protein-induced, previously unidentified twin form of calcite. *Proc. Natl. Acad. Sci. U.S.A.* **104**, 7337–7341 (2007).
34. J. P. Perdew, K. Burke, M. Ernzerhof, Generalized gradient approximation made simple. *Phys. Rev. Lett.* **77**, 3865–3868 (1996).
35. P. E. Blöchl, Projector augmented-wave method. *Phys. Rev. B Condens. Matter* **50**, 17953–17979 (1994).
36. H. J. Monkhorst, J. D. Pack, Special points for Brillouin-zone integrations. *Phys. Rev. B* **13**, 5188–5192 (1976).